

Comparison of Nitrate and Chloride Anions at the Air-Water Interface by Second
Harmonic Generation and Surface Tension

Thesis

Presented in Partial Fulfillment of the Requirements for the Degree Master of Science in
the Graduate School of The Ohio State University

By

Meredith Varnecky

Graduate Program in Chemistry

The Ohio State University

2021

Thesis Committee

Prof. Dr. Heather C. Allen, Advisor

Prof. Dr. Anne Co

Copyrighted by
Meredith Varnecky
2021

Abstract

Some of the most common ions in the atmosphere are nitrate (NO_3^-) and chloride (Cl^-) which play key roles in many atmospheric reactions, including ozone depletion.

Additionally, they influence the iron equilibria that dictate reaction kinetics.

Heterogeneous reactions are heavily influenced by the presence of ions at the air-water interface but there is still not a definitive distinction between the surface propensity of NO_3^- and Cl^- . The impact of NO_3^- and Cl^- on the hydrogen-bonding structure at the air-water interface has been examined using second harmonic generation (SHG) and surface tension measurements. The impact of ferric iron on the propensity of NO_3^- has also been examined with surface tension by comparison to sodium nitrate. The SHG electric field shows that the hydrogen-bonding structure of NaNO_3 and NaCl solutions is significantly different from neat water but shows a slightly different dependence on concentration.

Surface tension measurements support this change in structure by displaying significantly different concentration dependence. The introduction of iron has a large impact on the surface as shown by the increased surface tension slope as well. To confirm the presence of iron-anion dipoles, geometry optimization of ferric chloride complexes was performed to obtain dipole moments.

Dedication

To the friends I have made along the way

Acknowledgments

Firstly, I would like to thank my advisor, Dr. Heather C. Allen, for her encouragement in pursuing this degree. I would also like to thank Tehseen Adel and Ka Chon Ng for teaching and advising me throughout this process as well.

Vita

May 2019.....B.S. Chemistry, Christopher Newport University, Newport News, Virginia, USA

August 2019.....Graduate Teaching Associate, Department of Chemistry and Biochemistry, The Ohio State University – Columbus, Ohio, USA

Publications

Blackshaw, K. J.; Varmecky, M. G.; Patterson, J. D. Interfacial Structure and Partitioning of Nitrate Ions in Reverse Micelles. *J. Phys. Chem. A* **2019**, *123* (1), 336–342.
<https://doi.org/10.1021/acs.jpca.8b09751>.

Fields of Study

Major Field: Chemistry

Table of Contents

Abstract.....	ii
Dedication.....	iii
Acknowledgments.....	iv
Vita.....	v
List of Tables.....	viii
List of Figures.....	ix
Chapter 1. Introduction.....	1
1.1 Overview.....	1
1.2 Motivation.....	1
1.2.1 Chloride and nitrate in the atmosphere.....	1
1.2.2 Unique surface propensity.....	2
1.2.3 Interaction of chloride and nitrate with heavy metals.....	3
Chapter 2. Theory and Instrumentation.....	5
2.1 Second Harmonic Generation Spectroscopy.....	5
2.1.1 Polarizability of a Dipole Moment.....	5
2.1.2 Second Harmonic Generation (SHG).....	5
2.1.3 Selection Rules.....	7
2.2 Surface Tensiometry.....	7
2.2.1 Gibbs Adsorption.....	7
2.2.2 Surface Free Energy and Surface Tension.....	10
2.2.3 Wilhelmy Plate Measurement.....	10
2.3 Calculations of Dipole Moment.....	11
2.3.1 Basic Principle of Density-functional Theory.....	11
2.3.2 Polarizable Continuum Model.....	12
Chapter 3. Materials and Methods.....	14

3.1 Materials	14
3.2 Methods.....	14
3.2.1 Sample Preparation	14
3.2.2 Second Harmonic Generation Spectroscopy Instrumentation	16
3.2.3 Surface Tension	17
3.2.4 Dipole Moment Calculations	18
Chapter 4. Results and Discussion.....	19
4.1. SHG Intensity.....	19
4.2 Surface Tension	21
4.3 Dipole moments of FeCl ₃ aqueous complexes	23
Chapter 5. Conclusion.....	26
Bibliography	28

List of Tables

Table 1. Preparation of Individually Massed Iron Samples.....	15
Table 2. Preparation of Iron Samples from 2.84 m Stock Solution.....	16
Table 3. Dipole moments of FeCl ₃ complexes	24

List of Figures

Figure 1. (a) Geometry of SHG. (b) Energy-level diagram of SHG.....	6
Figure 2. Schematic representation of the second harmonic generation instrument.	17
Figure 3. (a) SHG intensity enhancement. (b) SHG electric field (square root of the SHG intensity) enhancement.	20
Figure 4. Change in surface tension with salt concentration.	22
Figure 5. Change in surface tension with ionic strength.....	23
Figure 6. Geometry of (a) $\text{FeCl}_2 \cdot 4\text{H}_2\text{O}^+$, (b) $\text{FeCl}_3 \cdot 3\text{H}_2\text{O}$, and (c) FeCl_4^-	25

Chapter 1. Introduction

1.1 Overview

One of the most prominent interfaces in the atmosphere is the air-water interface, found from aerosols to thin films. The ubiquitous chloride (Cl^-) and nitrate (NO_3^-) ions participate in many reactions at this interface such as the ozone-depleting cycles. These reactions are heavily influenced by the unique surface propensity of ions. Both NO_3^- and Cl^- have been shown to have a weak surface propensity but are believed to not be depleted at the interface. Both Cl^- and NO_3^- distort the interfacial hydrogen-bonding network, albeit through different interactions. Hydrogen bonding is at play between NO_3^- and its first hydration shell, whereas charge transfer between the anion and hydrating water molecules is more efficient with Cl^- .^{1,2} While there has been a study on the relative affinity stating that NO_3^- has a higher propensity than Cl^- , the difference between them is still not fully understood.³ These anions also impact atmospheric iron by forming complexes that impede reaction equilibria.

1.2 Motivation

1.2.1 Chloride and nitrate in the atmosphere

Some of the most abundant ions in the atmosphere are NO_3^- and Cl^- .⁴ Both play key roles in many atmospheric processes such as photolysis and heterogeneous reactions. Perhaps most notably is their potential as oxidant sources, especially the common OH radical.⁵

The presence of one of these ions can also impact reactions involving the other. An increased fraction of Cl^- increases the rate of photolysis from NO_3^- to NO_2 ,⁵ a major oxidant in the ozone-depleting NO_x cycle. In marine regions, the formation of NO_3^- depletes Cl^- via reaction with nitrate derivatives.⁶⁻⁸ Many of these reactions have been shown to occur, or even be enhanced, at the air-water interface.⁵

1.2.2 Unique surface propensity

Reactions that occur at this interface are described as heterogeneous reactions or reactions that occur between two different phases. It has been shown that ions present at this interface significantly influence the reaction kinetics.⁹ However, ions have unique propensities for the interface which is dependent on size and polarizability. The larger, heavier halides, iodide (I^-) and bromide (Br^-), have been shown to significantly perturb the hydrogen-bonding environment at the interface, evidence of their presence in the region. Fluoride (F^-) and Cl^- showed little change in this region in one study.¹ Simulations have given another perspective, showing that I^- and Br^- are preferentially adsorbed to the surface, I^- more so than Br^- , while Cl^- is neutrally adsorbed and F^- is repelled.⁹

Much like Cl^- , NO_3^- has been predicted to generally have a weak surface propensity in simulations, though there is some disagreement.¹⁰⁻¹⁴ However, NO_3^- has also been directly observed at the interface with vibrational sum frequency generation² and UV-second harmonic generation.¹⁵ Generally, it is predicted that NO_3^- has neither a surface excess or depletion compared to bulk. Though the propensity of NO_3^- and Cl^- have been predicted to be similar, the work by Tian et al. which used phase-sensitive sum-frequency

vibration spectroscopy to determine the relative surface propensity of several ions, determined that NO_3^- has a higher relative propensity than Cl^- .³

Aside from this finding, there is one crucial difference between these anions in the interface: while Cl^- has been shown to have little effect on the interfacial hydrogen-bonding structure except for charge transfer perturbation to the first hydration shell^{1,5}, NO_3^- clearly disrupts this environment.¹⁶ There are a few differences between these two anions that may be the reason behind their varied interactions with the interface. Firstly, while Cl^- and the other halides have a spherical structure, NO_3^- has a planar structure that may be distorted at the interface, as suggested by the appearance of the NO_3^- symmetric stretch noted by Xu et al.² Secondly, it has been observed that interfacial NO_3^- is dehydrated compared to the ion in bulk.¹⁴

1.2.3 Interaction of chloride and nitrate with heavy metals

Heavy metals also play a key in the atmosphere, iron being of particular interest due to its abundance from dust to anthropogenic sources like combustion of fossil fuels and its heavy influence on ocean biogeochemistry and, in turn, climate.¹⁷⁻²¹ NO_3^- and Cl^- commonly interact with atmospheric iron by forming complexes.²²⁻²⁴ A key difference between complexes with NO_3^- and Cl^- , for ferric iron at least, is that while Cl^- is directly bonded to the ferric center of the complex, also called the formation of a contact ion-pair, there is no evidence of such pairs for NO_3^- . Rather, the iron-nitrate complex is believed to be a solvent-shared ion-pair complex.²² The equilibrium between these complexes understandably has a significant effect on the kinetics of important atmospheric reactions like Fenton reactions. In Fenton chemistry, iron catalyzes the production of key

atmospheric oxidants from peroxides.^{25,26} A direct comparison of the effect of NO_3^- and Cl^- on Fenton reaction kinetics showed that for the oxidation of Fe(II) , both anions gave an equal rate of reaction. However, for the reaction of Fe(III) , Cl^- was a much more effective dampener than NO_3^- . These differences were attributed to the above-mentioned complex formation lowering iron availability for reaction and the scavenging of the OH radical to form the less reactive Cl_2^- radical.^{24,27}

Chapter 2. Theory and Instrumentation

2.1 Second Harmonic Generation Spectroscopy

2.1.1 Polarizability of a Dipole Moment

The electric field of light can induce a change in the dipole moment of a material. In linear optics, this induced polarization scales linearly with the strength of the electric field as

$$P(t) = \epsilon_0 \chi^{(1)} E(t) \quad (2.1.1)$$

Where $P(t)$ is the induced dipole moment per unit volume or polarization of the system at time t , ϵ_0 is the permittivity of free space, $\chi^{(1)}$ is the linear susceptibility of the system, and $E(t)$ is the strength of the applied field at time t . Eq. 2.1.1 can be expanded as a power series for nonlinear optics.

$$\begin{aligned} P(t) &= \epsilon_0 (\chi^{(1)} E(t) + \chi^{(2)} E^2(t) + \chi^{(3)} E^3(t) + \dots) \\ &\equiv P^{(1)}(t) + P^{(2)}(t) + P^{(3)}(t) + \dots \end{aligned} \quad (2.1.2)$$

In this expansion, $\chi^{(2)}$ and $\chi^{(3)}$ are the second- and third-order nonlinear optical susceptibilities, respectively, while $P^{(2)}(t)$ and $P^{(3)}(t)$ are the second- and third-order polarization.²⁸

2.1.2 Second Harmonic Generation (SHG)

For a laser beam with a frequency of ω at time t , the electric field strength can be written

$$E(t) = E e^{-i\omega t} + c. c. \quad (2.1.3)$$

Where $c.c.$ is the complex conjugate and E the magnitude of the field. When incident on a material with a non-zero $\chi^{(2)}$, $P^{(2)}(t)$ can be written explicitly as

$$P^{(2)}(t) = 2\epsilon_0\chi^{(2)}EE^* + (\epsilon_0\chi^{(2)}E^2e^{-i2\omega t} + c.c.) \quad (2.1.4)$$

There are two terms in this expression, the first contributing at zero frequency and the second at twice the frequency. This second term represents the second harmonic generation process where two photons of the same energy are converted to one at twice the energy when interacting with a non-centrosymmetric medium. This process is represented in Figure 1.^{28,29}

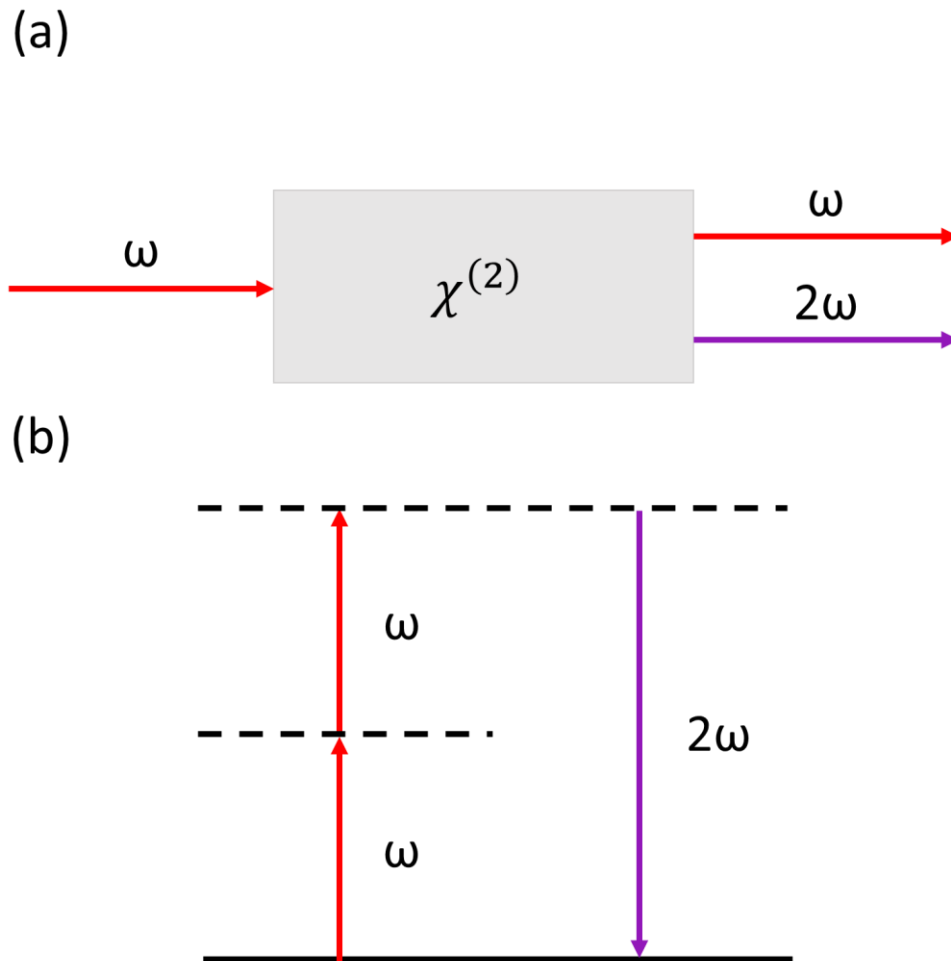


Figure 1. (a) Geometry of SHG. (b) Energy-level diagram of SHG.

2.1.3 Selection Rules

Second-order processes like SHG can only occur in non-centrosymmetric mediums as the second-order susceptibility must be nonzero to have a second-order response. In centrosymmetric mediums, the inversion operation changes the sign of the electric field but not $\chi^{(2)}$. Therefore, the polarization becomes

$$-P^{(2)}(t) = \epsilon_0 \chi^{(2)} (-E(t))^2 = \epsilon_0 \chi^{(2)} E(t)^2 = P^{(2)}(t) \quad (2.1.5)$$

For this equation to be true, $\chi^{(2)}$ must be zero. Therefore, the SHG intensity will also be zero as it is proportional to the $|\chi^{(2)}|^2$. While bulk phases are typically centrosymmetric, excluding certain crystal structures, this symmetry is broken at the interface, allowing the second-order process.^{28,29}

2.2 Surface Tensiometry

2.2.1 Gibbs Adsorption

Models of an interfacial system can be divided into three regions: two bulk phases (α and β) and the interface between them (σ). Gibbs' approach to this system defines the interface as an infinitesimally thin plane between the two homogeneous regions called the Gibbs dividing surface (GDS). For a real system, however, the interface has volume with changing thermodynamic properties as it goes from phase α to β with the bulk regions marked homogenous properties. The GDS can be placed arbitrarily within the inhomogeneous interface and the system's extensive properties – such as total internal energy (U), total Gibbs free energy (G), and the total number of the i -th substance (n_i) – treated as a sum of the three regions.

$$U = U^\alpha + U^\beta + U^\sigma \quad (2.2.1)$$

$$G = G^\alpha + G^\beta + G^\sigma \quad (2.2.2)$$

$$n_i = n_i^\alpha + n_i^\beta + n_i^\sigma \quad (2.2.3)$$

As the GDS has no volume, n_i^σ depends on the placement of the GDS. The difference between the ideal bulk values using the GDS and the real system is defined as surface excess. Surface excess can be expressed in terms of unit area with Eq. 2.2.4 where A is the area.

$$\Gamma_i^\sigma = \frac{n_i^\sigma}{A} \quad (2.2.4)$$

The change in energy of an interfacial system can be expressed by substituting Eq. 2.2.5, the thermodynamic definition of internal energy,

$$dU = TdS - PdV + \sum_{i=1}^N \mu_i dn_i + W \quad (2.2.5)$$

Where T is temperature, S is entropy, P is pressure, V is volume, μ_i is the chemical potential of the i-th component, and W is the non-PV work done on the system, into Eq. 2.2.1 to give Eq. 2.2.6

$$dU = \gamma dA - \sum_{\alpha,\beta} PdV + \sum_{\alpha,\beta,\sigma} (TdS + \sum_{i=1}^N \mu_i dn_i) \quad (2.2.6)$$

Where γ is the surface tension and dA the change in surface area. The interfacial component can be written as

$$dU^\sigma = TdS^\sigma + \gamma dA + \sum_{i=1}^N \mu_i dn_i^\sigma \quad (2.2.7)$$

Since the interface has no volume and, therefore, cannot perform volume work. It can perform work to change the surface area, which is represented by the surface work term, γdA . Integration of Eq. 2.2.7 while holding T, A and n_i^σ constant gives the more general Eq. 2.2.8 which can then be differentiated.

$$U^\sigma = TS^\sigma + \gamma A + \sum_{i=1}^N \mu_i n_i^\sigma \quad (2.2.8)$$

$$dU^\sigma = TdS^\sigma + S^\sigma dT + \sum_{i=1}^N \mu_i dn_i^\sigma + \sum_{i=1}^N n_i^\sigma d\mu_i + \gamma dA + Ad\gamma \quad (2.2.9)$$

Equating Eq. 2.2.7 and 2.2.9 gives

$$0 = S^\sigma dT + \sum_{i=1}^N n_i^\sigma d\mu_i \quad (2.2.10)$$

Or, per unit area

$$d\gamma = -S^\sigma dT - \sum_{i=1}^N \Gamma_i^\sigma d\mu_i \quad (2.2.11)$$

For a binary system at constant temperature, Eq. 2.2.11 can be written

$$d\gamma = -\Gamma_1^\sigma d\mu_1 - \Gamma_2^\sigma d\mu_2 \quad (2.2.12)$$

As surface excess is dependent on the GDS position, Γ_1^σ can be set to 0 to simplify Eq. 2.2.12 to Eq. 2.2.13.

$$\Gamma_2 = -\left(\frac{\delta\gamma}{\delta\mu_2}\right)_T \quad (2.2.13)$$

Differentiation of the definition of chemical potential,

$$\mu_2 = \mu_2^\circ + RT \ln(a_2) \quad (2.2.14)$$

Where μ_2° is the chemical potential of the standard state, R is the universal gas constant, and a_2 is the activity allows the substitution of Eq. 2.2.14 into Eq. 2.2.13 to give

$$d\mu_2 = RT \frac{da_2}{a_2} \quad (2.2.15)$$

$$\Gamma_2 = -\frac{a_2}{RT} \frac{d\gamma}{da_2} \quad (2.2.16)$$

Also known as the Gibbs Equation or Gibbs adsorption isotherm. This equation shows that, when the change in surface tension with concentration is positive, the solute is depleted from the interface.³⁰⁻³²

2.2.2 Surface Free Energy and Surface Tension

Gibb's free energy of the surface can be derived from the following thermodynamic relationship and Eq. 2.2.8.

$$dG = dU - TdS - SdT + PdV + VdP \quad (2.2.17)$$

Recall that the interface, under the Gibbs convention, cannot perform volume work and so the PdV term is equal to 0. Substitution of Eq. 2.2.8 into Eq. 2.2.17 gives

$$dG^\sigma = -S^\sigma dT + V^\sigma dP + \sum_{i=1}^N \mu_i dn_i^\sigma + \gamma dA \quad (2.2.18)$$

Which can be expressed as a sum of partial derivatives.

$$dG = \left(\frac{\delta G}{\delta T}\right)_{P,n_i,A} dT + \left(\frac{\delta G}{\delta P}\right)_{T,n_i,A} dP + \left(\frac{\delta G}{\delta n_i}\right)_{P,T,A} dn_i + \left(\frac{\delta G}{\delta A}\right)_{P,T,n_i} dA \quad (2.2.19)$$

Comparison of Eqs. 2.2.19 and 2.2.18 shows that

$$\gamma = \left(\frac{\delta G}{\delta A}\right)_{P,T,n_i} \quad (2.2.20)$$

Eq. 2.2.20 defines surface tension, then, as the work needed to change the surface area.

Physically, this means that surface tension is the reduction of surface area to minimize the energy at the surface. Molecules at the surface do not experience the net zero force of those in bulk, where molecules pull in all directions. Rather, surface molecules have a net force towards the bulk, reducing interfacial area.³⁰⁻³²

2.2.3 Wilhelmy Plate Measurement

A relatively simple method to measure surface tension is the Wilhelmy plate method where a flat plate is dipped through the surface of a liquid. The surface tension can be calculated from

$$dW = \gamma p \quad (2.2.21)$$

Where dW is the change in weight of the plate and p is the plate perimeter.³²

2.3 Calculations of Dipole Moment

2.3.1 Basic Principle of Density-functional Theory

In elementary quantum mechanics, information is obtained by operating on a system's wave function (Ψ). Schrodinger's equation (SE) for a many-electron system which is used to calculate this wave function is

$$[\hat{T} + \hat{V} + \hat{U}]\Psi(\mathbf{r}_1, \mathbf{r}_2, \dots, \mathbf{r}_N) = E\Psi(\mathbf{r}_1, \mathbf{r}_2, \dots, \mathbf{r}_N) \quad (2.3.1)$$

Where \hat{T} gives the kinetic energy of the electrons, \hat{V} the potential, and U the electron-electron interactions, the sum of which gives the Hamiltonian operator. Or, more explicitly

$$\left[\sum_i^N \left(-\frac{\hbar^2 \nabla_i^2}{2m} \right) + \sum_i v(\mathbf{r}_i) + \sum_{i < j} \frac{q^2}{|\mathbf{r}_i - \mathbf{r}_j|} \right] \Psi(\mathbf{r}_1, \mathbf{r}_2, \dots, \mathbf{r}_N) = E\Psi(\mathbf{r}_1, \mathbf{r}_2, \dots, \mathbf{r}_N) \quad (2.3.2)$$

Where $v(\mathbf{r}_i)$ is the potential acting on the i -th electron at electronic coordinate \mathbf{r} , N the number of electrons, and E the resulting eigenvalue. The only term to change when working with a polyatomic molecule is the potential function to account for the nuclear coordinates as well. To obtain the wavefunction, then, one chooses $v(\mathbf{r})$ to use in the SE to solve for Ψ . Where density-functional theory (DFT) differs from other methods, is the sequence of solving for Ψ . Instead of choosing a potential, an observable of Ψ called the electron density ($n(\mathbf{r})$) is calculated to give knowledge of Ψ and, therefore, $v(\mathbf{r})$.³³ This reduces the computational cost of many-electron systems in comparison to traditional Hartree-Fock methods as the wave-function complexity increases exponentially with the number of electrons while the number of variables in $n(\mathbf{r})$ is independent of system size. This is only possible through the Hohenberg-Kohn (HK) theorem which states that a

ground-state $n(\mathbf{r})_0$ must give a corresponding, unique ground state Ψ_0 that then reproduces $n(\mathbf{r})_0$ and a minimized energy (E_0). Any arbitrary $n(\mathbf{r})$ that is not $n(\mathbf{r})_0$ will only give energies above E_0 and so the system will make small steps on the potential energy surface (PES) to find the closest local minima, at which point the optimized geometry will have been reached. Such calculations are still intensive, so for practical use, the Kohn-Sham equations are utilized for simplification. These equations introduce a fictitious auxiliary system expressed in single-electron orbitals (ie. A non-interacting system) under a potential $v(\mathbf{r})_s$. Choosing $v(\mathbf{r})_s$ to be equivalent to the potential of the original system allows the minimization of the non-interacting system to reach the same solution as the interacting system. Thus, the density described by the complex interacting SE can be solved with a noninteracting SE.³³

2.3.2 Polarizable Continuum Model

The DFT method discussed above does not account for solvent effects. To simulate a surrounding solvent, a polarizable continuum model (PCM) places a molecule within a dielectric continuum of permittivity ϵ . The molecule is placed in a cavity defined by assigned Van der Waals' radii for each element such that it excludes solvent molecules and contains the largest part of the solute charge distribution. The charge distribution within the cavity polarizes the dielectric and is then polarized itself. The Conductor-like Screening Model (COSMO) calculates the charge density with respect to the chosen dielectric by scaling the charge density calculated at the infinite dielectric of a conductor. Initially calculating the charge density at infinity modifies the potential boundary

conditions at the cavity surface to allow the apparent surface charge to be determined by just the local electrostatic potential. The charge density at the finite dielectric is scaled by

$$\sigma(s) = f(\epsilon)\sigma^*(s) \quad 2.3.3$$

Where $\sigma(s)$ is the charge distribution at point s for the finite dielectric, $\sigma^*(s)$ is for the infinite dielectric, and $f(\epsilon)$ is the dielectric screening factor given by

$$f(\epsilon) = \frac{\epsilon-1}{\epsilon+k} \quad 2.3.4$$

Where k has been noted to be dependent on cavity shape and solute charge distribution but ultimately the choice has been shown to be irrelevant for water.^{34,35}

Chapter 3. Materials and Methods

3.1 Materials

The salts used were CTAB (Sigma Aldrich, 98%), SDS (Sigma Aldrich, 98%), $\text{Fe}(\text{NO}_3)_3 \cdot 9\text{H}_2\text{O}$ (Acros organics, $\geq 99\%$), NaNO_3 (Acros organics, $\geq 99\%$), and NaCl (Acros Organics, $\geq 99\%$). Pure water was obtained from a Milli-Q Advantage A10 with a resistivity of $18.2 \text{ M}\Omega\cdot\text{cm}$. Samples were prepared or diluted in Fisherbrand™ 20mL borosilicate glass scintillation vials. Materials for sample prep include Fisherbrand™ 20mL borosilicate glass scintillation vials, Air-Tite™ bulk unsterile syringes, and 0.2 μm PVDF Basix™ non-sterile syringe filters. Ammonium peroxydisulfate powder (Certified ACS) and sulfuric acid (Fisher Chemical, Certified ACS Plus) were used for cleaning.

3.2 Methods

3.2.1 Sample Preparation

Stock solutions of 0.03 mM CTAB and SDS were prepared in 1 L volumetric flasks. NaCl was baked for a minimum of 6 hours at 650°C in crucibles to remove contaminants and allowed to cool completely before the preparation of a 4.17 m NaCl stock solution. NaNO_3 stock solutions of the same concentration were syringe-filtered 3 times for the same purpose. These stock solutions were diluted to the desired concentration with pure water in 20 mL vials for most concentrations. The 2.00, 2.50, and 3.00 m NaCl solutions used in surface tension measurements were made by weighing the salt needed in 10 g of pure water for each sample. $\text{Fe}(\text{NO}_3)_3 \cdot 9\text{H}_2\text{O}$ was used as received. For the concentrations shown in Table 1, the iron salt was massed individually to a 20 mL vial and dissolved in pure water immediately prior to use to minimize aggregation.

Table 1. Preparation of Individually Massed Iron Samples

Sample Concentration (m)	Fe(NO₃)₃ · 9H₂O mass (g)	Water mass (g)
0.2	0.8080	9.6757
0.5	2.0200	9.1893
1	4.0400	8.3786
1.5	6.0600	7.5679
2	8.0800	6.7572
2.5	10.1000	5.9466
3	12.1200	5.1359

A stock solution of 2.84 m Fe(NO₃)₃ was used to prepare the concentrations shown in Table

2. All glassware was cleaned with an established method of immersion in an acidic solution prepared by dissolving 8 grams of ammonium peroxydisulfate powder per 500 mL of sulfuric acid. Glass was kept in the solution for a minimum of two hours and then rinsed thoroughly with pure water. It was then baked in an oven until dry.

Table 2. Preparation of Iron Samples from 2.84 m Stock Solution

Sample Concentration (m)	Fe(NO₃)₃ Stock Volume (mL)	Water Volume (mL)
0.0284	0.100	9.90
0.0568	0.200	9.80
0.114	0.400	9.60
0.170	0.600	9.40
0.227	0.800	9.20
0.284	1.00	9.00
0.568	2.00	8.00
0.852	3.00	7.00
1.14	4.00	6.00
1.42	5.00	5.00
1.70	6.00	4.00

3.2.2 Second Harmonic Generation Spectroscopy Instrumentation

The SHG instrument uses a Tsunami broad band Ti:Sapphire from Spectra-Physics centered at 805 nm with a bandwidth of 20 nm, a sub 50 fs pulse width, and an 82 MHz repetition rate. The laser beam is pumped by a Millennia Vs continuous-wave laser from Spectra-Physics with a pump power of 5.00 W. The Tsunami laser has an average output power of 850 mW and a power of 600 mW incident on the sample. Figure 2 shows the

instrument schematic, where the beam is split into reference and signal channels to monitor fluctuations in laser quality. Both channels are sent through a Shramrock SR303i monochromator and collected with an Andor Newton EMCCD (DU970P-BVF) at the same time. The signal is then calibrated to the measured reference. The calibrated values were normalized to the ratio of 1.0, which was fixed as the SHG signal of water. Measurements were made with p-polarized light for excitation and detection with an exposure time of 90 s. Solutions were analyzed in a glass Petri dish with a diameter of 3 cm. Four NaCl and two NaNO₃ trials were averaged.

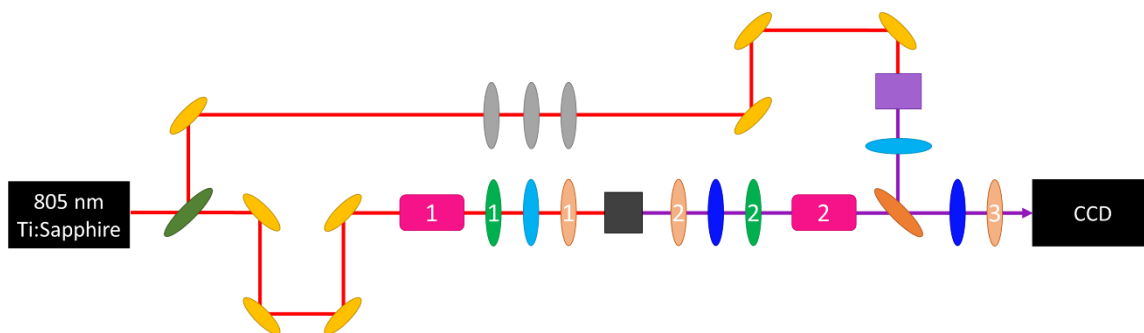


Figure 2. Schematic representation of the second harmonic generation instrument. The dark green oval is an 85/15 beam splitter. All yellow ovals are dielectric mirrors. Pink squares 1 and 2 are 800 and 405 nm Glan-laser polarizers, respectively. The first light green oval is an 800 nm achromatic half-wave plate and the second a 405 nm half-wave plate. The light orange ovals are the 75 mm, 100 mm, and 50 mm plano-convex lenses with anti-reflective coating for 650-1050 nm for 1, 2, and 3, respectively. 690 nm long-pass filters are represented by the light blue ovals while each dark blue oval represents two 785 nm short-pass filters. The dark orange oval is a silica plate, and the light gray ovals are neutral density filters. The dark gray box is the sample and the purple box the BBO crystal to give the second harmonic signal for the reference beam.

3.2.3 Surface Tension

Surface tension measurements were performed with a 0.02 m width platinum Wilhelmy plate with a Biolin Scientific Sigma 703 D force tensiometer. The plate was cleaned with ethanol and pure water then heated with a Bunsen burner until red hot. All measurements were made at atmospheric pressure, in a temperature range of 20-25°C and 20-30%

relative humidity. The plate was brought down until the first touch with the water surface in a petri dish and allowed to equilibrate for 60 s before recording the measurement. The plate was brought up, allowed to rest until measurements stopped changing, and brought back to first touch at a minimum of 4 times, 5 or more if the first measurements were not consistent to the last to ensure fluctuation had ceased. The water was replaced with a cleaned pipette tip that had only been used with lower concentrations of the same salt to ensure the concentration in the petri dish was not changed. The same measurement process was used for the salt, except the measurements were stopped after 4 touches to ensure equal equilibration time for each salt. The last measurement was taken as the “true” measurement for comparison of the salt to water. Measurements were reproduced in triplicate at a minimum.

3.2.4 Dipole Moment Calculations

The geometry of the iron chloride species was optimized under the COSMO³⁴ PCM model using the water dielectric of 78.39 and iron (III) Van der Waal’s radius of 2.04 Å.³⁶ These were computed at the B3LYP/def2-TZVP³⁷⁻³⁹ level with a D3 empirical dispersion correction⁴⁰ using the q-chem software, v. 5.3,⁴¹ to obtain the dipole moments for each iron species. All calculations were made with a sextet multiplicity.⁴²

Chapter 4. Results and Discussion

4.1. SHG Intensity

A comparison of the effect of chloride and nitrate on the air-water interface was made using SHG in Figure 3. The trendline intercept was set to 1 to represent the normalized water value. Both NaCl and NaNO₃ showed a linear increase in signal with concentration, though the NaNO₃ slope was slightly higher than NaCl. As the intensity is normalized with respect to water, it is clear that both salts enhance the intensity (Figure 3a.). It can be said, then, that the salts are increasing the electric field at the interface as the intensity is proportional to the square of the field (Figure 3b.). Both NaNO₃ and NaCl are non-resonant, meaning that they do not have an electronic transition at either the 800

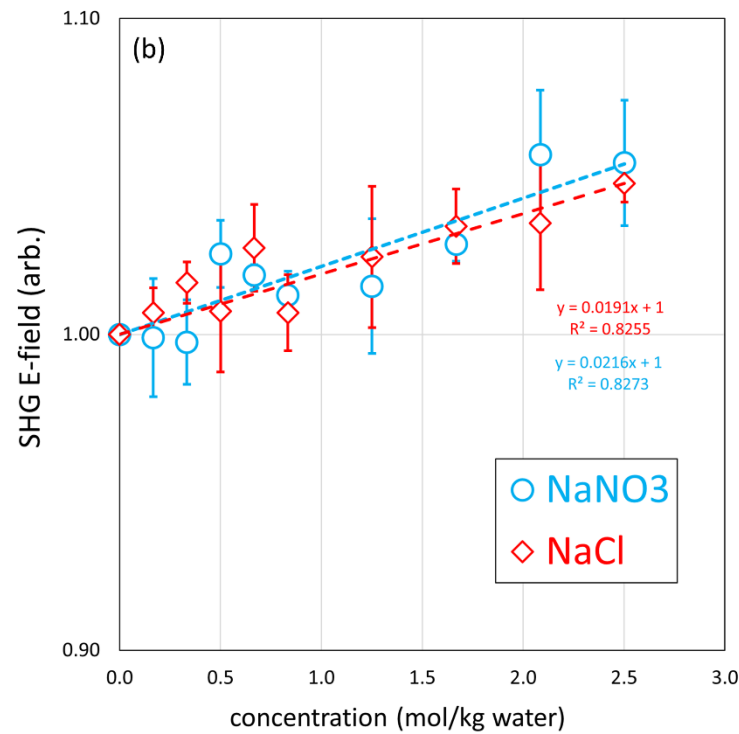
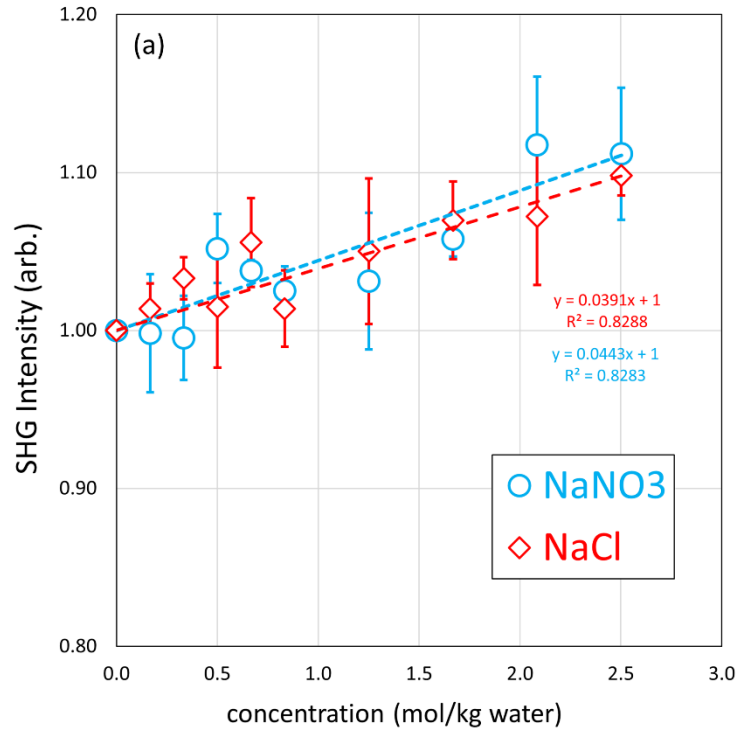


Figure 3. (a) SHG intensity enhancement. (b) SHG electric field (square root of the SHG intensity) enhancement.

or 400 nm wavelength of the incident or second harmonic light, the increase in intensity must be due to a change in the water structure rather than interaction with the ions. It has been proposed by Bian et al. that this change in intensity is due to an increase in interfacial thickness as the ions disrupt the hydrogen bonding network and puts more molecules in non-centrosymmetric environments.⁴³ This was supported by Liu et al. who suggested that the change in interfacial size increases with size and polarizability of the halides tested.¹ As NO_3^- has a larger polarizability than Cl^- ,² it would make sense that NO_3^- has a slightly larger change in intensity. However, Xu et al. found that this did not stay true for NO_3^- , as NO_3^- increased the Raman signal intensity of the ion solvation peak less than Cl^- . It was proposed that difference in anion structure, spherical halide versus planar NO_3^- , could account for this difference.²

4.2 Surface Tension

This difference was explored further by comparing the change in surface tension with concentration in Figure 4. NaCl has a larger slope than NaNO_3 , as shown by Pegram and Record,⁴⁴ which suggests that the hydrogen bonding environment is different between Cl^- and NO_3^- . NO_3^- may perturb the hydrogen bond structure more than Cl^- as it has a surface tension slope comparable to Br^- which has been shown to significantly perturb the surface environment.¹ The higher slope of NaCl than NaNO_3 suggests a higher depletion of anion at the surface. As with the SHG data, this could be caused by the difference in polarizability and/or the different anion structures.

The effect of Fe(III) on the interaction of NO_3^- with the surface was observed as well. The change from Na to Fe(III) gave a significant slope increase. This shows that the

introduction of Fe(III) greatly changes the surface propensity of NO_3^- , possibly caused by the formation of the solvent shared iron-nitrate complex. Thus, the iron-nitrate complex likely has a lower surface propensity than NO_3^- . As $\text{Fe}(\text{NO}_3)_3$ solutions are highly acidic, this is unusual since acids generally have a negative slope, or a surface excess.⁴⁴

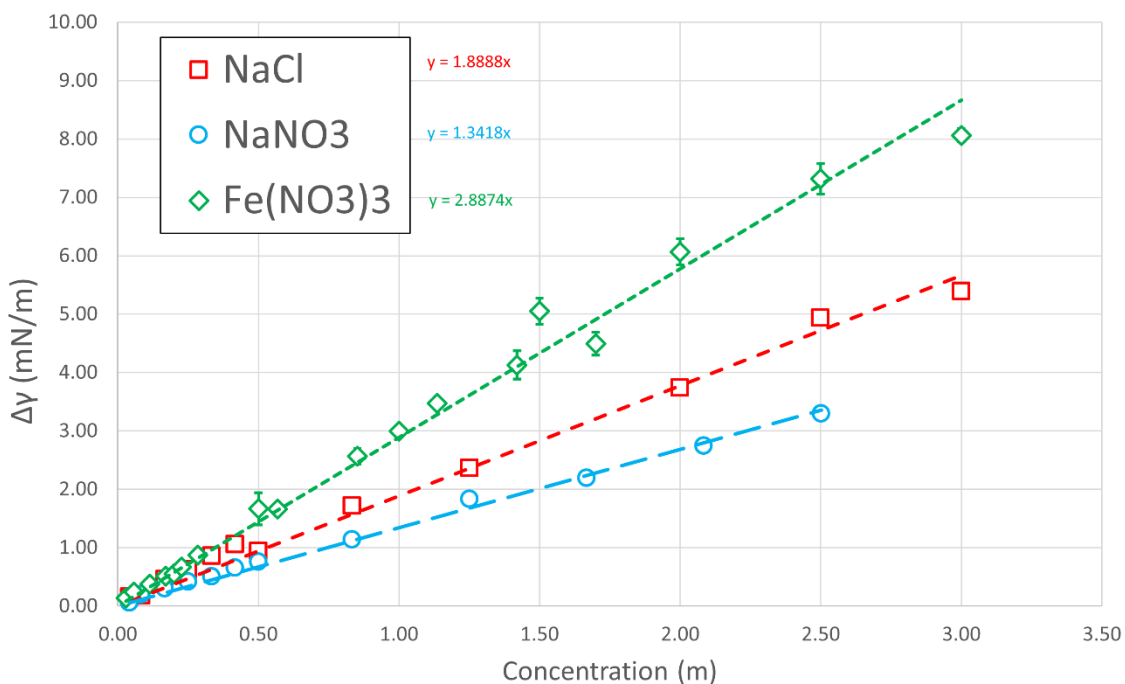


Figure 4. Change in surface tension with salt concentration.

A comparison of surface tension with ionic strength was made to account for the higher ratio of anions in the iron salt. In Figure 5, this comparison is made under the assumption that the number of ions is equivalent to the 1:3 ratio found in the $\text{Fe}(\text{NO}_3)_3$ salt – while not representative of a real solution with speciation, it is a starting point.

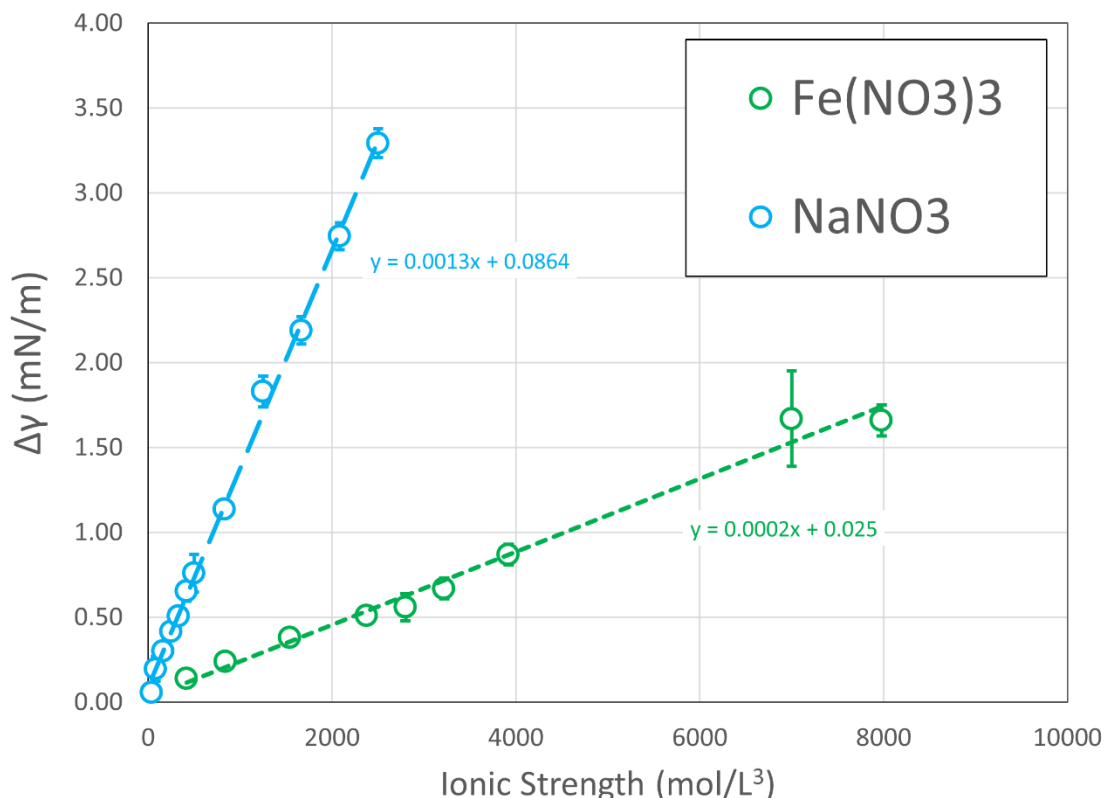


Figure 5. Change in surface tension with ionic strength.

Surface tension increases with ionic strength significantly faster for NaNO₃ than Fe(NO₃)₃. This could suggest that the difference due to cation choice in Figure 4 was not purely from changes in interactions but simply the higher concentration of ions.

4.3 Dipole moments of FeCl₃ aqueous complexes

The dipole moments of three FeCl₃ complexes were calculated from the optimized geometries, shown in Figure 6, to confirm the presence of dipoles that may interact with the surface. The calculated FeCl₂·4H₂O⁺ energy was -2490.13 hartrees which is lower than the -2182.08 hartrees calculated by Bach et al. for FeCl₂⁺ without a PCM. For the FeCl₃·3H₂O complex, the calculated energy was -2874.08 hartrees while Bach et al.'s energy for FeCl₃ was -2642.17 hartrees.⁴² As each set of these values are relatively close,

and the water introduced in this calculation lowered the energy, it can be concluded that these calculations are viable as the introduction of a solvent in which the molecules will spontaneously dissolve should lower the energy. The dipole moments are summarized in Table 3. The dipole moment of the one known $\text{Fe}(\text{NO}_3)_3$ complex was not calculated as its structure and solvation shell is not as well defined as the FeCl_3 complexes are.^{22,45}

Table 3. Dipole moments of FeCl_3 complexes

Dipole moment in:	X (Debye)	Y (Debye)	Z (Debye)	Total (Debye)
$\text{FeCl}_2 \cdot 4\text{H}_2\text{O}^+$	-1.28	2.55	-0.39	2.88
$\text{FeCl}_3 \cdot 3\text{H}_2\text{O}$	5.50	-4.54	0.15	7.14
FeCl_4^-	0.00	0.00	0.00	0.00

Understandably, FeCl_4^- has a dipole moment of 0 Debye as it has a tetrahedral structure with no complexed water molecules, thus the dipole moments cancel out. $\text{FeCl}_2 \cdot 4\text{H}_2\text{O}^+$ has a lower dipole moment than $\text{FeCl}_3 \cdot 3\text{H}_2\text{O}$, as one might expect since $\text{FeCl}_2 \cdot 4\text{H}_2\text{O}^+$ is more symmetric than $\text{FeCl}_3 \cdot 3\text{H}_2\text{O}$. Overall, Table 3 shows that iron species do have dipole moments that may interact with the surface and thus alter the surface tension and SHG signal of the solution compared to sodium salts like NaCl and NaNO_3 .

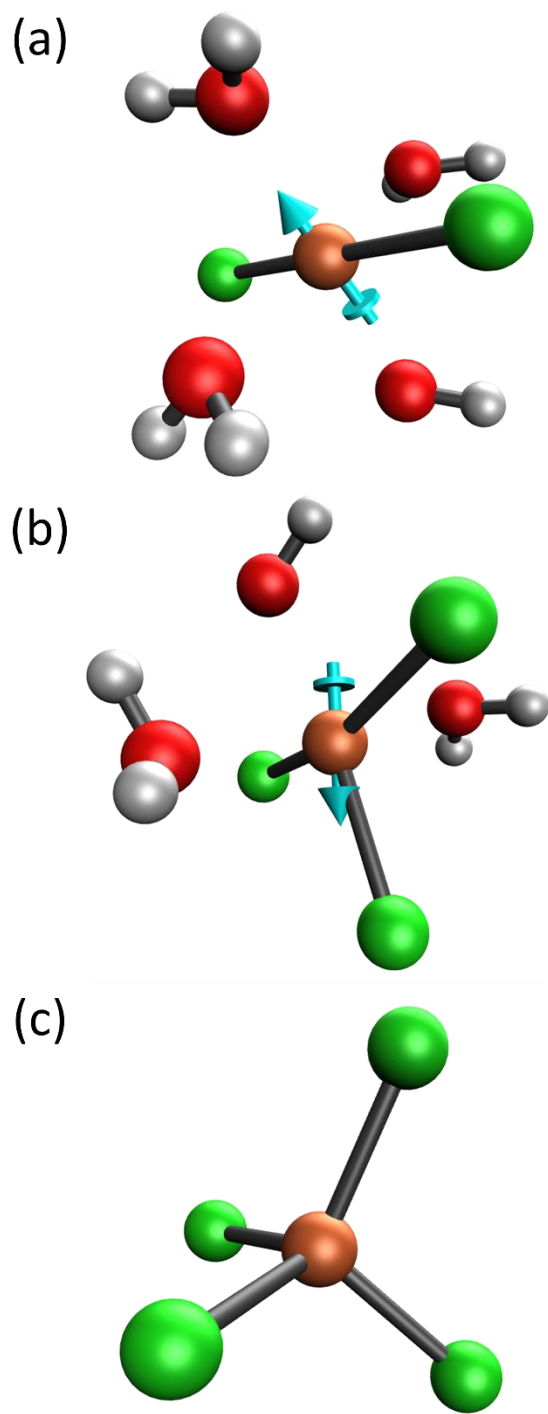


Figure 6. Geometry of (a) $\text{FeCl}_2 \cdot 4\text{H}_2\text{O}^+$, (b) $\text{FeCl}_3 \cdot 3\text{H}_2\text{O}$, and (c) FeCl_4^- .

Chapter 5. Conclusion

In this thesis, the effects of two ubiquitous atmospheric ions on the air-water interface were compared using SHG and surface tension. The effect of Fe(III), another ion with important atmospheric implications, on the interaction of NO_3^- with the surface was observed by the change in surface tension to sodium nitrate. The dipole moments of FeCl_3 aqueous species were calculated in place of the one undefined $\text{Fe}(\text{NO}_3)_3$ species structure to confirm the possible presence of dipoles that may interact with the interface as well.

Cl^- and NO_3^- showed similar effects on the SHG signal, though NO_3^- had a slightly larger rate of change with concentration. Meanwhile, Cl^- showed a significantly larger change in surface tension with concentration. Possible causes for these differences are the difference in polarizabilities and anion structure differences.

The introduction of Fe(III) to NO_3^- introduced the possibility of speciation to disrupt the interactions of NO_3^- at the surface, but also significantly increased the ionic strength of the solution with the 1:3 ratio of Fe(III) to NO_3^- . While surface tension increased with concentration more for $\text{Fe}(\text{NO}_3)_3$ than NaNO_3 , ionic strength showed the opposite trend. As the assumption in calculating the ionic strength was that the Fe: NO_3 ratio was 1:3, this was not representative of a real system but gives insight into the difference between the interactions of NO_3^- with sodium and Fe(III).

The three FeCl_3 species studied were $\text{FeCl}_2 \cdot 4\text{H}_2\text{O}^+$, $\text{FeCl}_3 \cdot 3\text{H}_2\text{O}$, and FeCl_4^- . Of these three, $\text{FeCl}_2 \cdot 4\text{H}_2\text{O}^+$ and $\text{FeCl}_3 \cdot 3\text{H}_2\text{O}$ had non-zero dipole moments which may interact with the interface.

Future work for this work would involve taking SHG measurements of the $\text{Fe}(\text{NO}_3)_3$ solutions. Comparison of these measurements with SHG and surface tension FeCl_3 measurements would provide further insight into the differences and effects between Cl^- and NO_3^- ions at aqueous surfaces.

Bibliography

- (1) Liu, D.; Ma, G.; Levering, L. M.; Allen, H. C. Vibrational Spectroscopy of Aqueous Sodium Halide Solutions and Air-Liquid Interfaces: Observation of Increased Interfacial Depth. *J. Phys. Chem. B* **2004**, *108* (7), 2252–2260. <https://doi.org/10.1021/jp036169r>.
- (2) Xu, M.; Tang, C. Y.; Jubb, A. M.; Chen, X.; Allen, H. C. Nitrate Anions and Ion Pairing at the Air-Aqueous Interface. *J. Phys. Chem. C* **2009**, *113* (6), 2082–2087. <https://doi.org/10.1021/jp805376x>.
- (3) Tian, C.; Byrnes, S. J.; Han, H.-L.; Shen, Y. R. Surface Propensities of Atmospherically Relevant Ions in Salt Solutions Revealed by Phase-Sensitive Sum Frequency Vibrational Spectroscopy. *J. Phys. Chem. Lett.* **2011**, *2* (15), 1946–1949. <https://doi.org/https://doi.org/10.1021/jz200791c>.
- (4) Finlayson-Pitts, B. J.; Pitts, J. *Chemistry of the Upper and Lower Atmosphere*; Academic Press, 2000.
- (5) Tobias, D. J.; Stern, A. C.; Baer, M. D.; Levin, Y.; Mundy, C. J. Simulation and Theory of Ions at Atmospherically Relevant Aqueous Liquid-Air Interfaces. *Annu. Rev. Phys. Chem.* **2013**, *64*, 339–359. <https://doi.org/10.1146/annurev-physchem-040412-110049>.
- (6) Finlayson-Pitts, B. J.; Pitts, J. N. Tropospheric Air Pollution: Ozone, Airborne Toxics, Polycyclic Aromatic Hydrocarbons, and Particles. *Science* (80-.). **1997**, *276* (5315), 1045–1052. <https://doi.org/10.1126/science.276.5315.1045>.
- (7) Finlayson-Pitts, B. J.; Hemminger, J. C. Physical Chemistry of Airborne Sea Salt Particles and Their Components. *J. Phys. Chem. A* **2000**, *104* (49), 11463–11472. <https://doi.org/10.1021/jp002968n>.
- (8) Finlayson-Pitts, B. J. The Tropospheric Chemistry of Sea Salt: A Molecular-Level View of the Chemistry of NaCl and NaBr. *Chem. Rev.* **2003**, *103* (12), 4801–4822. <https://doi.org/10.1021/cr020653t>.
- (9) Petersen, P. B.; Saykally, R. J. On the Nature of Ions at the Liquid Water Surface. *Annu. Rev. Phys. Chem.* **2006**, *57*, 333–364. <https://doi.org/10.1146/annurev.physchem.57.032905.104609>.
- (10) Salvador, P.; Curtis, J. E.; Tobias, D. J.; Jungwirth, P. Polarizability of the Nitrate Anion and Its Solvation at the Air/Water Interface. *Phys. Chem. Chem. Phys.* **2003**, *5* (17), 3752–3757. <https://doi.org/10.1039/b304537d>.
- (11) Minofar, B.; Vácha, R.; Wahab, A.; Mahiuddin, S.; Kunz, W.; Jungwirth, P. Propensity for the Air/Water Interface and Ion Pairing in Magnesium Acetate vs Magnesium Nitrate Solutions: Molecular Dynamics Simulations and Surface Tension Measurements. *J. Phys. Chem. B* **2006**, *110* (32), 15939–15944.

- <https://doi.org/10.1021/jp060627p>.
- (12) Jungwirth, P.; Tobias, D. J. Specific Ion Effects at the Air/Water Interface. *Chem. Rev.* **2006**, *106* (4), 1259–1281. <https://doi.org/10.1021/cr0403741>.
 - (13) Dang, L. X.; Chang, T. M.; Roeselova, M.; Garrett, B. C.; Tobias, D. J. On NO₃- - H₂O Interactions in Aqueous Solutions and at Interfaces. *J. Chem. Phys.* **2006**, *124* (6), 066101. <https://doi.org/10.1063/1.2171375>.
 - (14) Thomas, J. L.; Roeselová, M.; Dang, L. X.; Tobias, D. J. Molecular Dynamics Simulations of the Solution-Air Interface of Aqueous Sodium Nitrate. *J. Phys. Chem. A* **2007**, *111* (16), 3091–3098. <https://doi.org/10.1021/jp0683972>.
 - (15) Otten, D. E.; Petersen, P. B.; Saykally, R. J. Observation of Nitrate Ions at the Air/Water Interface by UV-Second Harmonic Generation. *Chem. Phys. Lett.* **2007**, *449*, 261–265. <https://doi.org/10.1016/J.CPLETT.2007.10.081>.
 - (16) Schnitzer, C.; Baldelli, S.; Shultz, M. J. Sum Frequency Generation of Water on NaCl, NaNO₃, KHSO₄, HCl, HNO₃, and H₂SO₄ Aqueous Solutions. *J. Phys. Chem. B* **2000**, *104* (3), 585–590. <https://doi.org/10.1021/jp9922231>.
 - (17) Jickells, T. D. Global Iron Connections Between Desert Dust, Ocean Biogeochemistry, and Climate. *Science* (80). **2005**, *308* (5718), 67–71. <https://doi.org/10.1126/science.1105959>.
 - (18) Falkowski, P. G.; Barber, R. T.; Smetacek, V. Biogeochemical Controls and Feedbacks on Ocean Primary Production. *Science* (80). **1998**, *281* (5374), 200–206. <https://doi.org/10.1126/science.281.5374.200>.
 - (19) Matsui, H.; Mahowald, N. M.; Moteki, N.; Hamilton, D. S.; Ohata, S.; Yoshida, A.; Koike, M.; Scanza, R. A.; Flanner, M. G. Anthropogenic Combustion Iron as a Complex Climate Forcer. *Nat. Commun.* **2018**, *9* (1), 1–10. <https://doi.org/10.1038/s41467-018-03997-0>.
 - (20) Sedwick, P. N.; Sholkovitz, E. R.; Church, T. M. Impact of Anthropogenic Combustion Emissions on the Fractional Solubility of Aerosol Iron: Evidence from the Sargasso Sea. *Geochemistry, Geophys. Geosystems* **2007**, *8* (10). <https://doi.org/10.1029/2007GC001586>.
 - (21) Takahashi, Y.; Furukawa, T.; Kanai, Y.; Uematsu, M.; Zheng, G.; Marcus, M. A. Seasonal Changes in Fe Species and Soluble Fe Concentration in the Atmosphere in the Northwest Pacific Region Based on the Analysis of Aerosols Collected in Tsukuba, Japan. *Atmos. Chem. Phys.* **2013**, *13* (15), 7695–7710. <https://doi.org/10.5194/acp-13-7695-2013>.
 - (22) Baumler, S. M.; Hartt, W. H.; Allen, H. C. Hydration of Ferric Chloride and Nitrate in Aqueous Solutions: Water-Mediated Ion Pairing Revealed by Raman Spectroscopy. *Phys. Chem. Chem. Phys.* **2019**, *21* (35), 19172–19180. <https://doi.org/10.1039/c9cp01392j>.
 - (23) Lin, L.; Husek, J.; Biswas, S.; Baumler, S. M.; Adel, T.; Ng, K. C.; Baker, L. R.; Allen, H. C. Iron(III) Speciation Observed at Aqueous and Glycerol Surfaces: Vibrational Sum Frequency and X-Ray. *J. Am. Chem. Soc.* **2019**, *141* (34), 13525–13535.
 - (24) De Laat, J.; Truong Le, G.; Legube, B. A Comparative Study of the Effects of Chloride, Sulfate and Nitrate Ions on the Rates of Decomposition of H₂O₂ and

- Organic Compounds by Fe(II)/H₂O₂ and Fe(III)/H₂O₂. *Chemosphere* **2004**, *55* (5), 715–723. <https://doi.org/10.1016/j.chemosphere.2003.11.021>.
- (25) Fischbacher, A.; von Sonntag, C.; Schmidt, T. C. Hydroxyl Radical Yields in the Fenton Process under Various PH, Ligand Concentrations and Hydrogen Peroxide/Fe(II) Ratios. *Chemosphere* **2017**, *182*, 738–744. <https://doi.org/10.1016/j.chemosphere.2017.05.039>.
- (26) Wardman, P.; Candeias, L. P. Fenton Chemistry: An Introduction. *Radiat. Res.* **1996**, *145* (5), 523–531. <https://doi.org/10.2307/3579270>.
- (27) De Laat, J.; Le, T. G. Effects of Chloride Ions on the Iron(III)-Catalyzed Decomposition of Hydrogen Peroxide and on the Efficiency of the Fenton-like Oxidation Process. *Appl. Catal. B Environ.* **2006**, *66* (1–2), 137–146. <https://doi.org/10.1016/j.apcatb.2006.03.008>.
- (28) Boyd, R. *Nonlinear Optics*, 3rd ed.; Academic Press, 2009.
- (29) Nihonyanagi, S.; Mondal, J. A.; Yamaguchi, S.; Tahara, T. Structure and Dynamics of Interfacial Water Studied by Heterodyne-Detected Vibrational Sum-Frequency Generation. *Annu. Rev. Phys. Chem.* **2013**, *64*, 579–603. <https://doi.org/10.1146/annurev-physchem-040412-110138>.
- (30) Birdi, K. S. Chattoraj, D. K. *Adsorption and The Gibbs Surface Excess*; Plenum Press, 1984.
- (31) Gaines, G. L. J. *Insoluble Monolayers at Liquid-Gas Interfaces*; Interscience Publishers, 1966.
- (32) Adamson, A. W. *Physical Chemistry of Surfaces*, 5th ed.; Wiley-Interscience, 1990.
- (33) Capelle, K. A Bird's-Eye View of Density-Functional Theory. In *Brazilian Journal of Physics*; Sociedade Brasileira de Fisica, 2006; Vol. 36, pp 1318–1341. <https://doi.org/10.1590/s0103-97332006000700035>.
- (34) Klamt, A.; Schüürmann, G. COSMO: A New Approach to Dielectric Screening in Solvents with Explicit Expressions for the Screening Energy and Its Gradient. *J. Chem. Soc. Perkin Trans. 2* **1993**, 799–805. <https://doi.org/10.1039/P29930000799>.
- (35) Tomasi, J.; Mennucci, B.; Cammi, R. Quantum Mechanical Continuum Solvation Models. *Chemical Reviews*. American Chemical Society 2005, pp 2999–3093. <https://doi.org/10.1021/cr9904009>.
- (36) Hu, S. Z.; Zhou, Z. H.; Robertson, B. E. Consistent Approaches to van Der Waals Radii for the Metallic Elements. *Zeitschrift fur Krist.* **2009**, *224* (8), 375–383. <https://doi.org/10.1524/zkri.2009.1158>.
- (37) Becke, A. D. Density-Functional Thermochemistry. III. The Role of Exact Exchange. *J. Chem. Phys.* **1993**, *98* (7), 5648–5652. <https://doi.org/10.1063/1.464913>.
- (38) Stephens, P. J.; Devlin, F. J.; Chabalowski, C. F.; Frisch, M. J. Ab Initio Calculation of Vibrational Absorption and Circular Dichroism Spectra Using Density Functional Force Fields. *J. Phys. Chem.* **1994**, *98* (45), 11623–11627. <https://doi.org/10.1021/j100096a001>.
- (39) Weigend, F.; Ahlrichs, R. Balanced Basis Sets of Split Valence, Triple Zeta

- Valence and Quadruple Zeta Valence Quality for H to Rn: Design and Assessment of Accuracy. *Phys. Chem. Chem. Phys.* **2005**, *7* (18), 3297–3305. <https://doi.org/10.1039/b508541a>.
- (40) Grimme, S.; Antony, J.; Ehrlich, S.; Krieg, H. A Consistent and Accurate Ab Initio Parametrization of Density Functional Dispersion Correction (DFT-D) for the 94 Elements H-Pu. *J. Chem. Phys.* **2010**, *132* (15), 154104. <https://doi.org/10.1063/1.3382344>.
- (41) Shao, Y.; Gan, Z.; Epifanovsky, E.; Gilbert, A. T. B.; Wormit, M.; Kussmann, J.; Lange, A. W.; Behn, A.; Deng, J.; Feng, X.; Ghosh, D.; Goldey, M.; Horn, P. R.; Jacobson, L. D.; Kaliman, I.; Khaliullin, R. Z.; Kuš, T.; Landau, A.; Liu, J.; Proynov, E. I.; Rhee, Y. M.; Richard, R. M.; Rohrdanz, M. A.; Steele, R. P.; Sundstrom, E. J.; Woodcock, H. L.; Zimmerman, P. M.; Zuev, D.; Albrecht, B.; Alguire, E.; Austin, B.; Beran, G. J. O.; Bernard, Y. A.; Berquist, E.; Brandhorst, K.; Bravaya, K. B.; Brown, S. T.; Casanova, D.; Chang, C. M.; Chen, Y.; Chien, S. H.; Closser, K. D.; Crittenden, D. L.; Diedenhofen, M.; Distasio, R. A.; Do, H.; Dutoi, A. D.; Edgar, R. G.; Fatehi, S.; Fusti-Molnar, L.; Ghysels, A.; Golubeva-Zadorozhnaya, A.; Gomes, J.; Hanson-Heine, M. W. D.; Harbach, P. H. P.; Hauser, A. W.; Hohenstein, E. G.; Holden, Z. C.; Jagau, T. C.; Ji, H.; Kaduk, B.; Khistyayev, K.; Kim, J.; Kim, J.; King, R. A.; Klunzinger, P.; Kosenkov, D.; Kowalczyk, T.; Krauter, C. M.; Lao, K. U.; Laurent, A. D.; Lawler, K. V.; Levchenko, S. V.; Lin, C. Y.; Liu, F.; Livshits, E.; Lochan, R. C.; Luenser, A.; Manohar, P.; Manzer, S. F.; Mao, S. P.; Mardirossian, N.; Marenich, A. V.; Maurer, S. A.; Mayhall, N. J.; Neuscamman, E.; Oana, C. M.; Olivares-Amaya, R.; Oneill, D. P.; Parkhill, J. A.; Perrine, T. M.; Peverati, R.; Prociuk, A.; Rehn, D. R.; Rosta, E.; Russ, N. J.; Sharada, S. M.; Sharma, S.; Small, D. W.; Sodt, A.; Stein, T.; Stück, D.; Su, Y. C.; Thom, A. J. W.; Tsuchimochi, T.; Vanovschi, V.; Vogt, L.; Vydrov, O.; Wang, T.; Watson, M. A.; Wenzel, J.; White, A.; Williams, C. F.; Yang, J.; Yeganeh, S.; Yost, S. R.; You, Z. Q.; Zhang, I. Y.; Zhang, X.; Zhao, Y.; Brooks, B. R.; Chan, G. K. L.; Chipman, D. M.; Cramer, C. J.; Goddard, W. A.; Gordon, M. S.; Hehre, W. J.; Klamt, A.; Schaefer, H. F.; Schmidt, M. W.; Sherrill, C. D.; Truhlar, D. G.; Warshel, A.; Xu, X.; Aspuru-Guzik, A.; Baer, R.; Bell, A. T.; Besley, N. A.; Chai, J. Da; Dreuw, A.; Dunietz, B. D.; Furlani, T. R.; Gwaltney, S. R.; Hsu, C. P.; Jung, Y.; Kong, J.; Lambrecht, D. S.; Liang, W.; Ochsenfeld, C.; Rassolov, V. A.; Slipchenko, L. V.; Subotnik, J. E.; Van Voorhis, T.; Herbert, J. M.; Krylov, A. I.; Gill, P. M. W.; Head-Gordon, M. Advances in Molecular Quantum Chemistry Contained in the Q-Chem 4 Program Package. *Mol. Phys.* **2015**, *113*, 184–215. <https://doi.org/10.1080/00268976.2014.952696>.
- (42) Bach, R. D.; Shobe, D. S.; Bernhard Schlegel, H.; Nagel, C. J. Thermochemistry of Iron Chlorides and Their Positive and Negative Ions. *J. Phys. Chem.* **1996**, *100* (21), 8770–8776. <https://doi.org/10.1021/jp953687w>.
- (43) Bian, H. T.; Feng, R. R.; Xu, Y. Y.; Guo, Y.; Wang, H. F. Increased Interfacial Thickness of the NaF, NaCl and NaBr Salt Aqueous Solutions Probed with Non-Resonant Surface Second Harmonic Generation (SHG). *Phys. Chem. Chem. Phys.* **2008**, *10* (32), 4920–4931. <https://doi.org/10.1039/b806362a>.

- (44) Pegram, L. M.; Record, M. T. Partitioning of Atmospherically Relevant Ions between Bulk Water and the Water/Vapor Interface. *Proc. Natl. Acad. Sci. U. S. A.* **2006**, *103* (39), 14278–14281. <https://doi.org/10.1073/pnas.0606256103>.
- (45) Flynn, C. M. Hydrolysis of Inorganic Iron(III) Salts. *Chemical Reviews*. American Chemical Society 1984, pp 31–41. <https://doi.org/10.1021/cr00059a003>.